

Tailoring Robust Quantum Anomalous Hall Effect via Entropy-Engineering

Syeda Amina Shabbir, Frank Fei Yun, Muhammad Nadeem,* and Xiaolin Wang†

Institute for Superconducting and Electronic Materials (ISEM),

Faculty of Engineering and Information Sciences (EIS),

University of Wollongong, Wollongong, New South Wales 2525, Australia

Development of quantum materials and tailoring of their functional properties is a fundamental interest in materials science. Here we propose a new design concept for robust quantum anomalous Hall effect via entropy engineering in 2D magnets. As a prototypical example, configurational entropy of monolayer transition metal trihalide VCl_3 is manipulated by incorporating four different transition-metal cations [Ti, Cr, Fe, Co] in the honeycomb structure made of vanadium, such that all the in-plane mirror symmetries, inversion and/or roto-inversion are broken. Monolayer VCl_3 is a ferromagnetic Dirac half-metal in which spin-polarized Dirac dispersion at valley momenta is accompanied by bulk states at the Γ -point and thus the spin-orbit interaction driven quantum anomalous Hall phase does not exhibit fully gapped bulk band dispersion. Entropy-driven bandstructure renormalization, especially band flattening in combination with red and blue shifts at different momenta of the Brillouin zone and crystal-field effects, transforms Dirac half-metal to a Dirac spin gapless semiconductor and leads to a robust quantum anomalous Hall phase with fully gapped bulk band dispersion, and thus, a purely topological edge state transport without mixing with dissipative bulk channels. These findings provide a paradigm to design entropy-driven 2D materials for the realization of robust quantum anomalous Hall effect and quantum device applications.

Keywords: High entropy materials, Spin gapless semiconductors, Dirac half-metals, 2D magnetic materials, Transition-metal halides, Quantum anomalous Hall effect, Topological transport.

I. INTRODUCTION

Spin-gapless semiconductors (SGSs) [1, 2] are characterized by gapless dispersion in one of the spin sectors while a gapped spectrum in the other spin sector. With this unique characteristic, SGSs bridge the gap between magnetic semiconductors [3] and magnetic half-metals [4, 5]. SGSs also serve as a fundamental ingredient for theoretical understanding and experimental realization of various exotic quantum phases such as the quantum anomalous Hall (QAH) effect [2, 6, 7], new (quantum) anomalous spin Hall effects [8], and topological nodal line spin-gapless semimetals [2, 9]. In addition, because of their intriguing electronic, magnetic and optical features, SGSs are promising candidates for quantum device applications, both with conventional bulk transport in tunneling junctions featuring large spin filtering and high tunneling magnetoresistance and with dissipationless topological edge state transport [2, 10–14].

After the seminal proposal for SGSs in 2008 [1], SGSs have been predicted in a variety of materials classes [2]. However, the experimental realization of SGSs and spin-orbit interaction (SOI) driven QAH effect has been hindered on several fronts. For instance, while indirect SGSs with parabolic dispersion have been confirmed, experimental confirmation of direct SGSs with Dirac/parabolic dispersion is limited. Similarly, other than intrinsic SGSs, various QAH materials have been fabricated and characterized, but with low Curie temperature, small topological bandgap, and the presence of

dissipative channels along the dissipationless chiral edge states. These challenges can be evaded with experimentally accessible direct SGSs where intrinsic magnetism and SOI could open a topologically nontrivial bandgap featuring a robust QAH effect. The search for direct SGSs and the corresponding high-temperature (Curie) robust QAH effect motivates bandstructure engineering in half-metallic magnets and magnetic semiconductors.

Here we propose a new design concept for SGSs through entropy engineering. Entropy engineering is a new concept of materials design rendering the entropy-dominated phase stabilization and tailoring of functional properties [15–18]. Due to the direct bandgap closing and an inherent connection of Dirac half-metals (DHMs) with Dirac SGSs (DSGSs), we consider monolayer vanadium trichloride VCl_3 as a material platform and manipulated its configurational entropy by incorporating four different transition metal (TM) atoms [M' : Ti, Cr, Fe, Co] in the honeycomb structure formed by vanadium cations, as shown in figure 1(a,b). The M' cations are substituted by vanadium atoms such that all in-plane mirror symmetries, inversion, and/or roto-inversion, are broken. Entropy-dominated effects on the electronic and spintronic properties of entropic $V_{0.5}(TiCrFeCo)_{0.5}Cl_3$ monolayer are studied using first-principles calculations. The entropy manipulation results in several intriguing features, such as band flattening due to red and blue shifts at different momenta of the Brillouin zone and a momentum shift of Dirac points due to the modification of in-plane crystal fields, as shown in Figure 1 (c, d, e). As a consequence of band flattening and crystal-field effects, VCl_3 monolayer undergoes a major bandstructure renormalization. First, renormalization of the entropy-driven band structure transforms the DHM

* mnadeem@uow.edu.au

† xiaolin@uow.edu.au

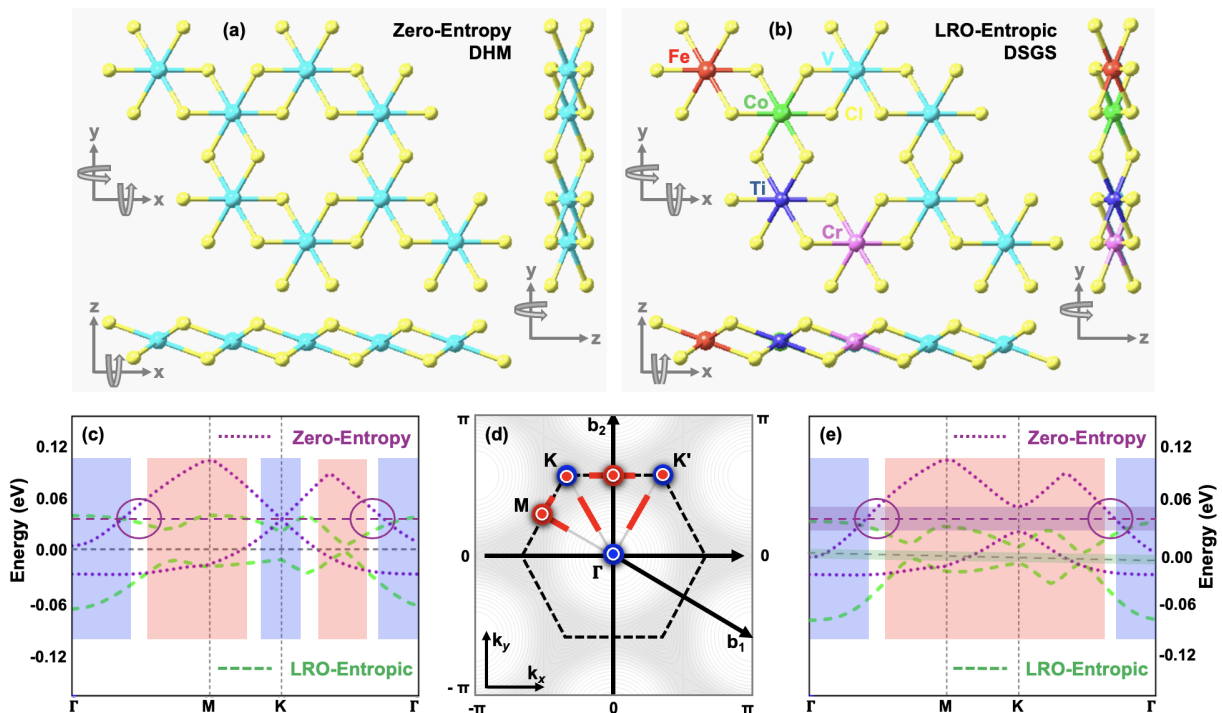


FIG. 1. **Design concept and bandstructure renormalization via entropy engineering.** (a, b) Lattice structure of zero entropy $(\text{VCl}_3)_8$ monolayer (a) and entropic $\text{TiV}_4\text{CrFeCoCl}_{24}$ monolayer (b) with top and side views. (c-e) Low-energy Dirac bands of zero-entropy VCl_3 monolayer (purple) and entropic $\text{TiV}_4\text{CrFeCoCl}_{24}$ monolayer (green) without SOI (c) and with SOI (e). Here red and blue regions, respectively, represent entropy-driven red and blue shift in the energy spectrum. Hexagonal shape first Brillouin zone showing red and blue shift at/along high symmetry points/lines where large (small) spheres indicate red/blue shift in the absence (presence) of SOI (d). While energy shift remains red and blue across M and Γ points, respectively, the energy dispersion across valleys K/ K' exhibit a blue shift in the absence of SOI while a red shift in the presence of SOI.

phase in the VCl_3 monolayer to a DSGS phase in the entropic $\text{V}_{0.5}(\text{TiCrFeCo})_{0.5}\text{Cl}_3$ monolayer, referred here as high-entropy DSGS (HE-DSGS). Second, when SOI is activated, a nontrivial bandgap leads to a robust QAH phase in $\text{V}_{0.5}(\text{TiCrFeCo})_{0.5}\text{Cl}_3$ monolayer. The robustness of the QAH phase is derived from the bandstructure renormalization. That is, a maximal blue shift at the Γ -point disentangles chiral edge states lying in the QAH gap from the bulk states and thus assures dissipationless chiral edge state topological transport.

II. METHODS AND RESULTS

All the computations are performed using the Vienna ab initio simulation package (VASP) [19, 20] within the generalized gradient approximation (GGA), employing the Perdew-Burke-Ernzerhof (PBE) exchange correlation functional [21]. Electronic and nuclear interactions are explained using the projector augmented wave (PAW) [22] technique. The energy criterion is set to 10^{-5} eV, while the atom force convergence is equal to 0.01 eV \AA^{-1} . Moreover, a PW (plane wave) kinetic energy cutoff is set to 500 eV. A $2 \times 2 \times 1$ supercell is built with vacuum spacing equal to 15 \AA along the normal direction so that

inter-layer interaction is prevented. The Brillouin zone was sampled using a $2 \times 2 \times 1$ and $11 \times 11 \times 1$ Gamma-centered Monkhorst-Pack grids [23] for optimization and electronic structure calculations. The unfolding of bands in VCl_3 2×2 supercell is performed using the VASP band unfolding package, VaspBandUnfolding [24]. In addition, orbital-resolved band structures are calculated using vaspkit software [25] and wanniertools software package is used to calculate edge states [26].

Configurational entropy (S_{conf}) is a controllable parameter, and the ‘level of entropy’ within the high entropy matrix could be tuned to achieve desired system functionalities. That is, an interplay between a global disorder and a local disorder allows to explore materials’ space exhibiting on-demand functional properties. It is important to note that neither a high configurational entropy measuring a degree of disorder nor a compositional complexity relying on diverse cations/anions could necessarily enhance functionalities, but a local environment determines material’s electronic and magnetic properties via local interactions. In a high-entropy configuration, the cation sites are randomly occupied by five or more TM atoms with equiatomic ratios such that $S_{\text{conf}} \geq 1.5R$, where R is the gas constant. The presence of clustering, phase separation, short-range ordering (SRO), or

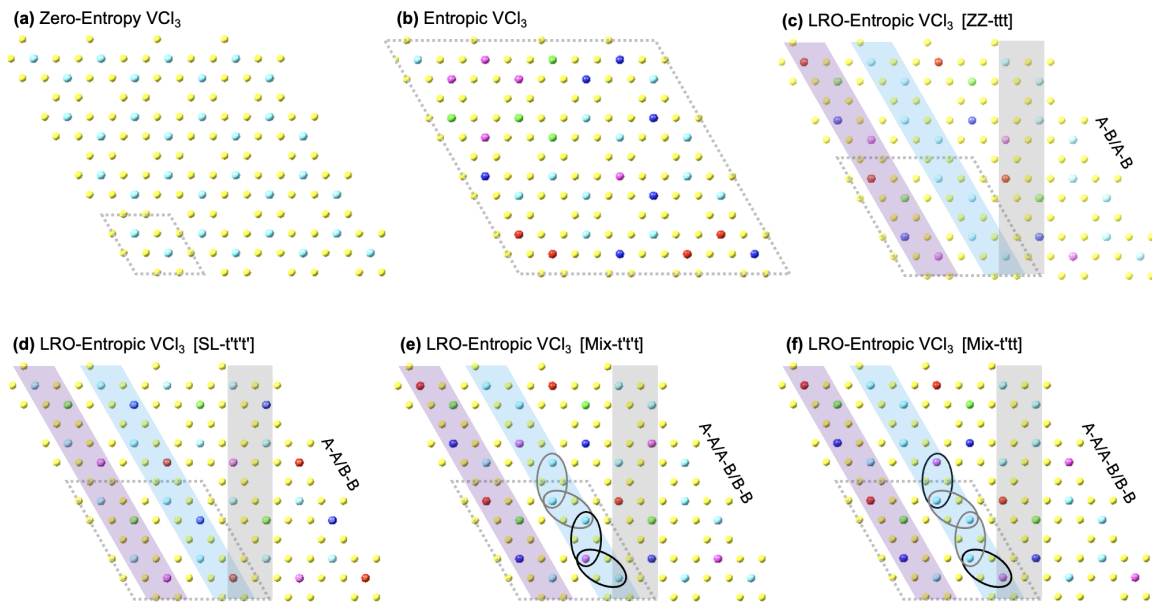


FIG. 2. **Entropic VCl_3 monolayer with a long-range order.** (a,b) A 4×4 supercell of zero-entropy VCl_3 (a) and maximal entropic VCl_3 with a random distribution of TM atoms at A and B sublattice sites of honeycomb structure, without a long-range order (b). (c,d) A 4×4 supercell of LRO-entropic VCl_3 with a long-range order along zigzag chains with A-B/A-B bonds favored by V/M' atoms (c) and a long-range order on sublattice sites with A-A/B-B bonds favored by V/M' atoms (d). (e,f) A 4×4 supercell of LRO-entropic VCl_3 with a mixed preference of A-A/A-B/B-B bonds by V/M' atoms. Panel (f) is same as panel (e), with an exchange of V and Cr sublattice sites, enclosed by black ovals. Here t and t' , respectively, represent nearest-neighbor hopping amplitude along V-V/M'-M' bonds and V-M' bonds. The t -triplet represent the pattern of nearest-neighbor hopping along zigzag chains, represented by blue and purple strips. Here vertical gray strips represent the armchair chains.

long-range ordering (LRO), lowers the entropy level from its maximal value, which is due to complete randomness, to its intermediate ($1R \geq S_{\text{conf}} < 1.5R$) or low ($0 < S_{\text{conf}} < 1R$) values.

Here we consider the VCl_3 monolayer as a prototypical 2D half-metallic ferromagnet and its configurational entropy is increased by substituting four vanadium atoms by TM atoms [M': Ti, Cr, Fe, Co], as shown in figure II. The highest level of entropy is derived from a random distribution of TM atoms at the A and B sublattice sites of the honeycomb structure, figure II(b). The entropy level of $V_{0.5}(\text{TiCrFeCo})_{0.5}Cl_3$ monolayer lowers from its maximal value when the system stabilizes with the LRO. As shown in figure II(c-f), four distinct long-ranged ordered entropic configurations of $V_{0.5}(\text{TiCrFeCo})_{0.5}Cl_3$ monolayer are studied, displaying an ordering of V/M atoms along (i) zigzag chains with A-B/A-B bonds favored by V/M' atoms, (ii) sublattice sites with A-A/B-B bonds favored by V/M' atoms, and (iii-iv) a long-range ordered entropic VCl_3 with a mixed preference of A-A/A-B/B-B bonds by V/M' atoms. These LRO-entropic configurations are labeled as ZZ-ttt, SL-t'tt', Mix-t'tt, and Mix-t'tt where t and t' represent the amplitude of nearest-neighbor hopping along V-V/M'-M' bonds and V-M' bonds, respectively. The t -triplet represents a pattern of nearest-neighbor hopping between sublattice sites along zigzag chains.

A. VCl_3 Monolayer

The monolayer of VCl_3 possess a buckled trilayered structure Cl-V-Cl with V atoms sandwiched between Cl atoms, where V atoms form a hexagonal honeycomb structure in which V^{3+} cations are covalently bonded to six nearest neighboring Cl^- anions. Each of the Cl^- anions is bonded to two V^{3+} cations via edge sharing octahedral coordination. Full geometry optimization is carried out on the unit cell of the unchanged VCl_3 monolayer to relax the structure. The optimized lattice constant obtained is 6.28 \AA , which is in good agreement with those previously reported for VCl_3 monolayer [14, 27–29] and VCl_3 crystal [30].

The VCl_3 monolayer is a ferromagnetic DHM [27, 28]; characterized by a Dirac point around the Fermi level [27] and an intrinsic long-range ferromagnetic character with estimated Curie temperatures up to 425 K [28]. It has been shown, through first-principle calculations, that the electronic and magnetic properties of VCl_3 monolayer can be tuned through single-atom substitutional doping with 3d TM atoms (Sc, Ti, Cr, Mn, Fe) [29]. It has also been demonstrated, via first-principle calculations combined with nonequilibrium Green's function, that a magnetic tunnel junction made of $VCl_3/CoBr_3/VCl_3$ exhibits a perfect spin filtering effect and a high tunnel

magnetoresistance ratio ($\approx 4.5 \times 10^{12}\%$) [14].

Despite all these interesting electronic and magnetic properties, however, VCl_3 monolayer does not guarantee a robust QAH phase, which is evident from the spin-polarized band dispersion, as shown in figure 1(c,e). The pristine monolayer VCl_3 is a DHM, characterized by a Dirac dispersion in the spin-up channel and a large indirect bandgap of > 4.5 eV in the spin-down channel. However, the Dirac point lying above the Fermi level at valley momenta (K/K') is accompanied by bulk states crossing the Fermi level at the Γ -point. This behavior has also been confirmed through the non-vanishing density of states at the Fermi level [28]. As a result, as shown in the figure 1(e), SOI opens a nontrivial bandgap at valleys but the bulk states at the Γ -point are further lowered and thus mix with the chiral edge states lying inside the nontrivial QAH gap. That is, even though spin-orbit coupled VCl_3 monolayer exhibits the QAH phase with a SOI-induced bandgap of 29 meV in the vicinity of valleys [27], the QAH phase in VCl_3 monolayer does not remain robust due to mixing of edge states with dissipative bulk states, a problem that also remains inevitable in magnetic doped topological insulators [2, 7, 31].

We also performed first-principle calculations for a 2×2 supercell of VCl_3 monolayer that is comprised of four unit cells, as shown in figure 1 (a). The electronic and magnetic properties of VCl_3 2×2 supercell remain same as that obtained for VCl_3 primitive cell, as shown in figure S1. That is, spin-polarized band dispersion of VCl_3 2×2 supercell also exhibits ferromagnetic Dirac half-metallic character, though with several additional bands. In addition, consistent with calculations performed over VCl_3 primitive cell, SOI opens a nontrivial QAH bandgap at valley momenta, which is same in magnitude to that obtained for VCl_3 primitive cell. However, similar to the VCl_3 primitive cell, bulk states in the vicinity of Γ -point lie inside the QAH gap. It reveals that the band dispersion of VCl_3 2×2 supercell is mere a folding of VCl_3 1×1 unit cell. This was further confirmed by unfolding the 2×2 band structure to reproduce the original VCl_3 band structure by using a VASP band unfolding procedure. The consistency of folding and unfolding of band dispersion in momentum-space is consistent with extrapolation in the real-space, i.e., 2×2 supercell of VCl_3 is simply an extrapolation of VCl_3 unit cell along x- and y-directions, as shown in figure 1 (a).

B. Entropic $\text{V}_{0.5}(\text{TiCrFeCo})_{0.5}\text{Cl}_3$ Monolayer

In the LRO-entropic VCl_3 with LRO along zigzag chains [ZZ-ttt], as shown in figure 1 (b) and II (c), the M' atoms are incorporated along zigzag chains such that the lattice structure is constituted by adjacent zigzag chains made of V-atoms and M' -atoms (Ti, Cr, Fe, Co) respectively. The geometric optimization of entropic $\text{V}_{0.5}(\text{TiCrFeCo})_{0.5}\text{Cl}_3$ 2×2 supercell shows that the optimized lattice constants remain the same as that of pris-

tine VCl_3 2×2 supercell. However, the atomic positions/coordinates of both TM and Cl atoms are considerably changed. As shown in figure 1 and 3, the entropy-driven bandstructure renormalization is featured by several interesting aspects such as band flattening, red and blue shifts at different momenta of the Brillouin zone, and a momentum shift of Dirac points. In the absence of SOI, figure 1(c) and 3(g), band flattening is a consequence of a blue shift in the vicinity of high-symmetry Γ -point and valleys K/K' while a red shift around the M-point and momenta along the $K-\Gamma$ symmetry line. While the blue shift opens a trivial gap at the Dirac points K/K' , the red shift at momenta k and k' along the symmetry lines $K-\Gamma$ and $K'-\Gamma$ induces Dirac points at the Fermi level. As a result, Dirac points move away from valleys (K/K') indicating an entropy-driven renormalization of crystal field effects.

In addition, unlike the zero-entropy VCl_3 monolayer in which the Dirac point lies above the Fermi level at the K-point while additional bulk states cross the Fermi level at the Γ -point, the Dirac point in the LRO-entropic VCl_3 [ZZ-ttt] lies exactly at the Fermi level (with a negligible gap of 6.6 meV) and the low-energy states at the Γ -point move away from the Fermi level. As a result, with an increase in entropy, VCl_3 monolayer is transformed from a DHM to a DSGS. The remarkable aspect of doping is that, while the entropy of the material has increased, the fermi energy has decreased sustaining the SGS Dirac point. This indicates that the electron density would have decreased. The decrease would likely be a result of electrons localization around the doped ions. This is confirmed through the calculated Fermi energy and bader charges.

SOI opens a nontrivial bandgap at the k/k' points along the $K/K' - \Gamma$ symmetry line featuring the QAH effect, as shown in figure 1(e). The emergence of chiral edge states in 1D dispersion, figure 4(b), validates the nontrivial bulk-boundary correspondence characterizing bulk states by non-vanishing Chern number $\mathcal{C} = \pm 1$. Interestingly, unlike the half-metallic VCl_3 monolayer in which the spin-polarized Dirac dispersion at the valley momenta is accompanied by bulk states at the Γ -point and thus the QAH phase does not remain fully gapped, figure 4(a), the LRO-entropic VCl_3 monolayer [ZZ-ttt] allows a fully gapped QAH phase and thus a purely topological edge state transport without mixing with dissipative bulk channels. The realization of DSGS phase and the robustness of corresponding QAH phase are associated with an entropy-driven band flattening in combination with red and blue shifts at different momenta of the Brillouin zone. However, unlike a blue shift in the absence of SOI, an increase in entropy induces a red shift around valley momenta in the spin-orbit coupled case. As a result, size of the nontrivial bandgap in the entropic case is smaller than the bandgap in the zero-entropy case. In a fully gapped and robust QAH phase in LRO-entropic VCl_3 , the bulk bandgap could be tuned via a suitable selection of TM atoms with the assurance

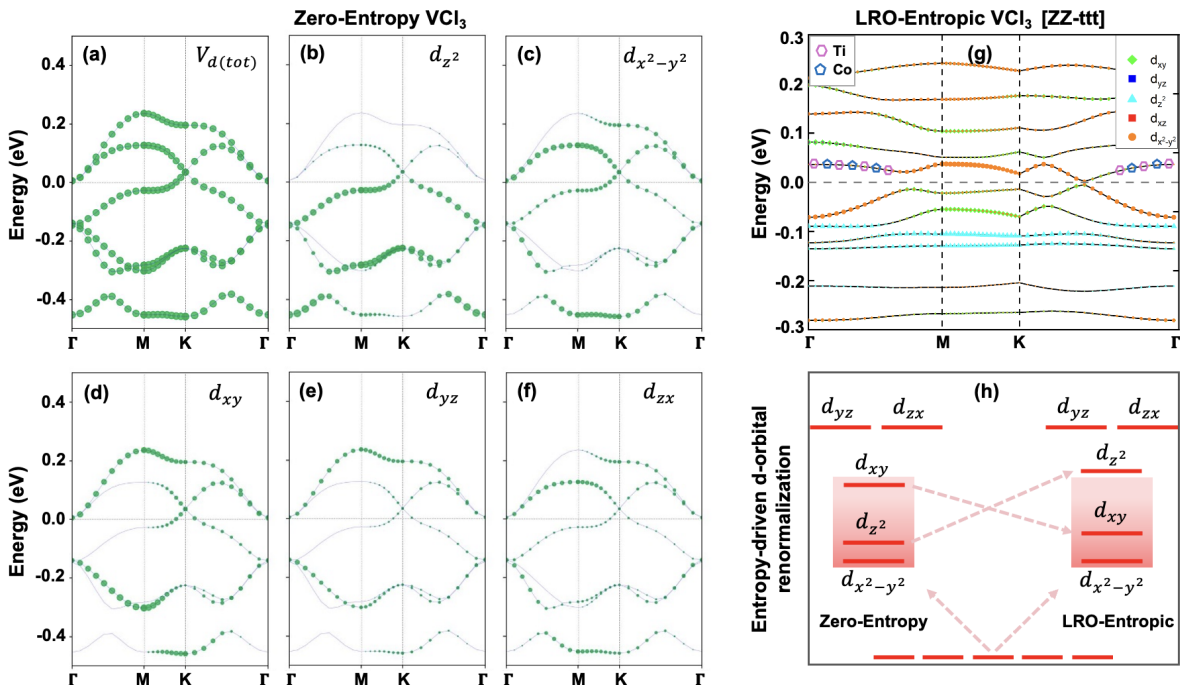


FIG. 3. **2D electronic dispersion and bandstructure renormalization.** (a-f) Orbital-resolved band dispersion of pristine VCl₃ monolayer (1 × 1 unit cell) showing total contributions of 3d-orbitals of vanadium (a), contribution from e_g orbitals (d_{z²}, d_{x^{2-y²}₂) (b,c) and t_{2g} orbitals (d_{xy}, d_{yz}, d_{zx}) (d,e,f). (g) Orbital-resolved band dispersion of entropic VCl₃ monolayer (2 × 2 supercell) showing contribution from 3d-orbitals of vanadium M' cations (Ti and Co). (h) A schematic representation of 3d-orbital renormalization of vanadium. The size of the bands represents the orbital weight.}

of a blue shift at both Γ and K/K' points.

To further investigate entropy-driven bandstructure renormalization and the effects of symmetry breaking, LRO-entropic cases SL-t't't', Mix-t't't', and Mix-t'tt are also analyzed. As shown in figure II(d-f), along with the redistribution of TM atoms, nearest-neighbor hopping matrix elements are also modified. As a consequence, the electronic dispersion also gets drastically modified from that of the LRO-entropic ZZ-ttt case. As shown in figure S2, the LRO-entropic chiral structure SL-t't't' displays a gapped dispersion also in the spin-up sector and thus featuring a ferromagnetic insulating phase, Mix-t't't' displays a nodal-line semi-metallic character between a spin-up and spin-down low-energy bands, while Mix-t'tt is a ferromagnetic insulator with a nearly flat band across Fermi level. Further details on the electronic and magnetic properties of these LRO-entropic cases are discussed in the Supplementary Information.

C. Orbital-Resolved Band Dispersion

In order to understand the microscopic origin of entropy-driven bandstructure renormalization, especially band flattening leading to the transition from half-metallic character to spin gapless semiconducting behavior and the accompanied effects on ferromagnetic ground

state, orbital resolved band dispersion of LRO-entropic V_{0.5}(TiCrFeCo)_{0.5}Cl₃ monolayer [ZZ-ttt] is investigated, as shown in figure 3. Due to the entropy-induced symmetry breaking, the bandstructure renormalization could originate from various effects at the microscopic level such as energy-splitting and redistribution of V-3d orbitals, contribution of spin-up electrons from the substituted TM-dopants, p-d hybridization between orbitals of Cl-atoms and TM-atoms, and the contribution of various TM-atoms to the total moment of magnetic ground state.

The pristine structure of VCl₃ stabilizes in ferromagnetic ground state with a total magnetic moment of $\approx 4.0 \mu_B$ per unit cell, where each V atom contributes $\approx 2.0 \mu_B$ while the magnetic moment of the surrounding Cl atoms is negligible. The ferromagnetic nature remains persistent for the 2 × 2 supercell displaying a total magnetic moment of $\approx 16.0 \mu_B$. These electronic and magnetic properties of the pristine monolayer VCl₃ are consistent with previously reported first-principle calculations [27–29]. Like the half-metallic VCl₃ monolayer, the ground state of the LRO-entropic monolayer [ZZ-ttt] remains ferromagnetic; however, the total magnetic moment is reduced to $10.9729 \mu_B$. The reduction in total magnetic moment is consistent with a phase transition from the DHM phase to a DSGS phase, in an itinerant ferromagnetic ground state.

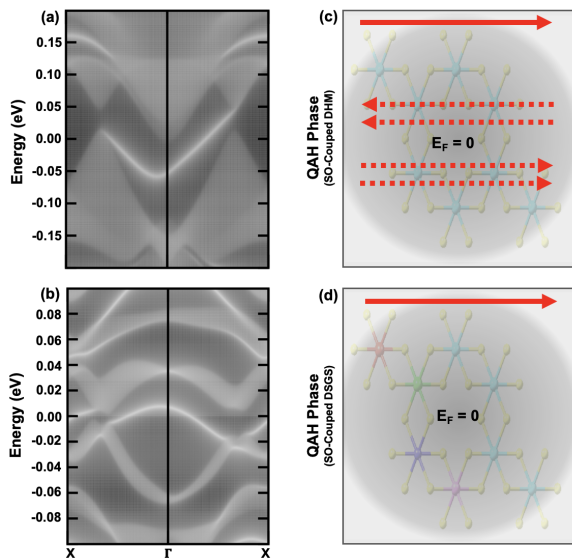


FIG. 4. **1D electronic dispersion and bulk-boundary correspondence.** (a, b) 1D band structure of zero-entropy VCl_3 monolayer (1x1 unit cell) (a) and entropic VCl_3 monolayer (2x2 supercell) with LRO along zigzag chains (b) showing chiral edge state in the momentum space. (c, d) A real space schematic representation of chiral edge state (solid arrow) and bulk modes (dashed arrow) crossing the Fermi level $E_f = 0$ in zero-entropy VCl_3 monolayer (c) and entropic VCl_3 monolayer with LRO along zigzag chains (d).

As shown in figure 3(a-f) and **S3**, the intrinsic half-metallicity in the VCl_3 monolayer is dominated by the vanadium 3d orbitals, with a negligible contribution from the Cl-p orbitals. The low-energy Dirac bands are predominantly occupied by e_g orbitals (d_{z^2} and $d_{x^2-y^2}$) and a d_{xy} orbital with a contribution from the d_{yz} and d_{zx} orbitals around the Γ -point. The orbital contribution to low-energy Dirac bands is in good agreement with previous first-principles studies on the VCl_3 monolayer [27, 29]. In addition to octahedral crystal field splitting of 3d-orbitals into a doublet e_g (d_{z^2} and $d_{x^2-y^2}$) and a triplet t_{2g} (d_{xy} , d_{yz} and d_{zx}), transition-metal trihalide monolayers with P31m symmetry could exhibit further splitting in the t_{2g} triplet such that low energy states are contributed by a singlet $e_{out}(d_{z^2})$ and a doublet $d_{in}(d_{xy}, d_{x^2-y^2})$ [32].

Like zero-entropy VCl_3 monolayer, spin-up bands of LRO-entropic monolayer [ZZ-ttt] are also predominantly occupied by a doublet $d_{in}(d_{xy}, d_{x^2-y^2})$ and a singlet $e_{out}(d_{z^2})$, as shown in figure 3 (g). However, there are several interesting modifications induced by enhanced configurational entropy. First, the low-energy Dirac bands are constituted by doublet d_{in} while the contribution of e_{out} to the Dirac bands is completely depleted. It shows that only in-plane 3d orbitals (d_{in}) contribute to the spin-up Dirac bands around the Fermi level, while the contribution from 3d-orbitals that extend along the out-of-plane direction (d_{yz} , d_{zx} , d_{z^2}) is diminished with

an increase in the entropy, leading to a red shift around the M-point and along the K- Γ line. The entropy-driven redistribution of 3d-orbitals is depicted in figure 3 (h). Second, the contribution from V atoms to a low-energy conduction band is significantly reduced at the Γ -point. On the other hand, as displayed in figure 3(g) and **S4**(b, c), contribution of Ti and Co to the low-energy conduction band is prominent at the Γ -point. In addition, as shown in figure **S4**(d,e), the contribution from Fe and Cr atoms is vanishingly small to the low-energy valence bands. As a result, the bulk states move away from the Fermi level; a blue shift at the Γ -point, leading to the DHM-DSGS phase transition. Such an entropy-driven depletion of V-3d orbitals with weight along the z-axis and a finite contribution from doped M' atoms (Ti and Co) causes a band flattening due to red and blue shifts at various momenta of the Brillouin zone.

In addition, unlike the zero-entropy VCl_3 monolayer, a contribution of Cl-p orbitals is enhanced in the LRO-entropic [ZZ-ttt] monolayer, as shown figure **S4**(f), leading to a hybridization between spin-up d-orbitals of TM atoms and spin-down p-orbitals of Cl atoms. Such p-d hybridization has also been predicted in Mn- and Fe-doped VCl_3 monolayers [29]. The p-d hybridization can further be validated by inspecting a reduction in magnetic moments of V-3d orbitals. In the zero-entropy VCl_3 monolayer, our first principle calculations show that each V^{3+} [$3d^2$] atom contributes a magnetic moment of $m_B = +1.918 \mu_B$ while each Cl^- atom contributes $m_B \approx -0.03 \mu_B$, as shown in table 1 of Supplementary Information. In the LRO-entropic monolayer [ZZ-ttt], on the other hand, while two of V atoms contribute $m_B \approx +1.90 \mu_B$, the magnetic moment of the other two V atoms reduces to $m_B \approx +1.80 \mu_B$ and that of Cl atoms varies from $m_B \approx -0.001 \mu_B$ to $m_B \approx -0.03 \mu_B$.

The coupling between the TM-3d orbitals and the surrounding Cl-p orbitals also affects the magnetic moments of TM-atoms, leading to a ferromagnetic ground state with a total magnetic moment of $m_B \approx +10.9729 \mu_B$, much smaller than the magnetic moment of zero-entropy case ($\approx 16 \mu_B$). Interestingly, unlike an antiferromagnetic coupling $\text{Cl}\downarrow\text{-TM}\uparrow\text{-Cl}\downarrow$ between the local magnetic moments of Cl atoms and TM atoms (V, Ti, Co, and Cr), a negative value of the local magnetic moment of the Fe cation indicates a ferromagnetic coupling $\text{Cl}\downarrow\text{-Fe}\downarrow\text{-Cl}\downarrow$ of the Fe atom with neighboring Cl atoms. This shows that entropy engineering could also be a promising design concept to control magnetic textures in real space. As shown in table 2 of Supplementary Information, doped TM atoms in a high-entropy environment exhibit characteristics that are distinct from doping of individual TM atoms in a low-entropy doped VCl_3 [29]. Further details about the magnetic moments of individual TM atoms and local spin textures for various LRO-entropic configurations are summarized in the Supplementary Information.

The renormalization of electronic and magnetic properties of LRO-entropic $\text{V}_{0.5}(\text{TiCrFeCo})_{0.5}\text{Cl}_3$ monolayer

[ZZ-ttt] shows that an interplay between electrons localization and de-localization emerges as a trademark of entropy engineering. While band flattening suggests that the decrease in the bandwidth is a direct consequence of entropy manipulation that reduces the inter-orbital overlap, a considerable contribution from Cl atoms and the reduced magnetic moments of TM atoms constituting low-energy bands indicate a hybridization between the d-orbitals of TM atoms and the p-orbitals of the surrounding Cl atoms. It shows that the LRO-entropic monolayer [ZZ-ttt] is a special case where nearest-neighbor hopping on the zigzag chains made of V-atoms predominantly constitutes low-energy Dirac bands, while the entropy level raised by doped M' atoms reduces the bandwidth of Dirac bands.

III. CONCLUSION AND OUTLOOK

Bandstructure renormalization and energy splitting of low-lying orbitals through entropy engineering are attributed to structural symmetry breaking caused by TM dopants in transition-metal trihalides [29, 33]. In addition, apart from the level of entropy and the nature of symmetry breaking, the electronic and magnetic properties of entropic materials rely on what elements are contributing to the low-energy bands and how their low-lying orbitals are influenced by the nearest-neighbor environments. In order to understand the impact of the nearest-neighbor environment on the electronic and magnetic properties, we systematically changed the sublattice site position of doped TM atoms with parent V atoms while keeping the level of entropy fixed. Our first-principle calculations show that a small change in the nearest-neighbor environment could lead to a significant change in electronic and magnetic properties.

A robust QAH effect is a unique feature of SGSs [2, 7], i.e., SOI opens a nontrivial energy gap by lifting the only twofold degeneracy of the Dirac point(s) in the bulk band dispersion that corresponds to the fully spin-polarized chiral modes in the edge state spectrum. In 2D magnets, the electronic transition from ferromagnetic DHM to a ferromagnetic DSGS and thus a robust QAH effect could

open a new route to revolutionize low-energy and high-performance electronic and spintronic technologies, such as giant magnetoresistance devices [2, 4, 34] overcoming the Schmidt obstacle [35, 36] and topological switching devices [2, 37–39] overcoming the Boltzmann tyranny [2, 40–44]. Although the entropy-driven QAH phase is robust, i.e., chiral edge states are completely disentangled from the bulk modes, the QAH gap in entropic VCl_3 is smaller than the QAH gap in zero-entropy VCl_3 . This reduction in the nontrivial bandgap is consistent with the role of SOI and the Berry curvature which capitalize on their maximal strength at valley points. It motivates further research to find suitable TM atoms that could reduce the crystal-field effect and enhance the nontrivial bandgap via blue shift at Dirac points, leading to a room-temperature realization of topological quantum device applications.

The proposed concept for materials design and discovery of DSGSs through entropy engineering, employed here for VCl_3 monolayer, could also be extended for other 2D DHMs and 2D Dirac materials. For instance, like VCl_3 monolayer, intrinsic magnetism [33], spin gapless electronic structure, and the corresponding SOI-induced QAH effect could be renormalized in various other monolayers of transition metal trihalides such as $OsCl_3$ [45], RuX_3 (X:Br,Cl,I)[46], MnX_3 (X:F,Cl,Br,I)[47], $NiCl_3$ [48], $PtCl_3$ [49], $PdCl_3$ [50], MBr_3 (M:Pd,Pt)[51], MBr_3 (M:V,Fe,Ni,Pd) [52], FeX_3 (X:Cl,Br,I)[53], and VX_3 (X:Cl,I)[14, 27–29]. Similarly, the proposed design concept could also be employed for enhancing the robustness of QAH phase in magnetic-doped topological insulators, i.e., dissipative bulk channels, and thus backscattering can be removed by increasing the configurational entropy.

ACKNOWLEDGMENTS

This research was supported by the Australian Research Council (ARC) Centre of Excellence in Future Low-Energy Electronics Technologies (FLEET), Project No. CE170100039, Discovery Project No. DP230102221, and Linkage Project No. LP220100085.

-
- [1] X. L. Wang, Proposal for a new class of materials: spin gapless semiconductors, *Physical review letters* **100**, 156404 (2008).
 - [2] M. Nadeem and X. Wang, Spin gapless quantum materials and devices, *Advanced Materials* **36**, 2402503 (2024).
 - [3] J. Kossut and W. Dobrowolski, Diluted magnetic semiconductors, *Handbook of Magnetic Materials* **7**, 231 (1993).
 - [4] R. De Groot, F. Mueller, P. v. van Engen, and K. Buschow, New class of materials: half-metallic ferromagnets, *Physical review letters* **50**, 2024 (1983).
 - [5] H. Van Leuken and R. De Groot, Half-metallic antiferromagnets, *Physical review letters* **74**, 1171 (1995).
 - [6] F. D. M. Haldane, Model for a quantum hall effect without landau levels: Condensed-matter realization of the "parity anomaly", *Physical review letters* **61**, 2015 (1988).
 - [7] M. Nadeem, A. R. Hamilton, M. S. Fuhrer, and X. Wang, Quantum anomalous hall effect in magnetic doped topological insulators and ferromagnetic spin-gapless semiconductors—a perspective review, *Small* **16**, 1904322 (2020).
 - [8] X.-L. Wang, Dirac spin-gapless semiconductors: promising platforms for massless and dissipationless spintronics and new (quantum) anomalous spin hall effects, *National*

- Science Review **4**, 252 (2017).
- [9] G. Ding, J. Wang, H. Chen, X. Zhang, and X. Wang, Investigation of nodal line spin-gapless semiconductors using first-principles calculations, *Journal of Materials Chemistry C* **10**, 6530 (2022).
- [10] E. Şaşıoğlu, S. Blügel, and I. Mertig, Proposal for reconfigurable magnetic tunnel diode and transistor, *ACS Applied Electronic Materials* **1**, 1552 (2019).
- [11] E. Şaşıoğlu, T. Aull, D. Kutschabsky, S. Blügel, and I. Mertig, Half-metal–spin-gapless-semiconductor junctions as a route to the ideal diode, *Physical review applied* **14**, 014082 (2020).
- [12] T. Aull, E. Şaşıoğlu, N. Hinsche, and I. Mertig, Ab initio study of magnetic tunnel junctions based on half-metallic and spin-gapless semiconducting heusler compounds: Reconfigurable diode and inverse tunnel-magnetoresistance effect, *Physical Review Applied* **18**, 034024 (2022).
- [13] N. Maji and T. K. Nath, Demonstration of reconfigurable magnetic tunnel diode and giant tunnel magnetoresistance in magnetic tunnel junctions made with spin gapless semiconductor and half-metallic heusler alloy, *Applied Physics Letters* **120** (2022).
- [14] Y. Feng, X. Wu, and G. Gao, High tunnel magnetoresistance based on 2d dirac spin gapless semiconductor vcl3, *Applied Physics Letters* **116** (2020).
- [15] B. S. Murty, J.-W. Yeh, S. Ranganathan, and P. Bhattacharjee, *High-entropy alloys* (Elsevier, 2019).
- [16] A. Sarkar, Q. Wang, A. Schiele, M. R. Chellali, S. S. Bhattacharya, D. Wang, T. Brezesinski, H. Hahn, L. Velasco, and B. Breitung, High-entropy oxides: fundamental aspects and electrochemical properties, *Advanced Materials* **31**, 1806236 (2019).
- [17] W.-L. Hsu, C.-W. Tsai, A.-C. Yeh, and J.-W. Yeh, Clarifying the four core effects of high-entropy materials, *Nature Reviews Chemistry* , 1 (2024).
- [18] S. Schweidler, M. Botros, F. Strauss, Q. Wang, Y. Ma, L. Velasco, G. Cadilha Marques, A. Sarkar, C. Kübel, H. Hahn, *et al.*, High-entropy materials for energy and electronic applications, *Nature Reviews Materials* **9**, 266 (2024).
- [19] G. Kresse and J. Hafner, Ab initio molecular dynamics for liquid metals, *Physical review B* **47**, 558 (1993).
- [20] G. Kresse and D. Joubert, From ultrasoft pseudopotentials to the projector augmented-wave method, *Physical review b* **59**, 1758 (1999).
- [21] J. P. Perdew, K. Burke, and M. Ernzerhof, Generalized gradient approximation made simple, *Physical review letters* **77**, 3865 (1996).
- [22] P. E. Blöchl, Projector augmented-wave method, *Physical review B* **50**, 17953 (1994).
- [23] H. J. Monkhorst and J. D. Pack, Special points for brillouin-zone integrations, *Physical review B* **13**, 5188 (1976).
- [24] Q. Zheng, Pyvaspwfc, <https://github.com/QijingZheng/VaspBandUnfolding> (2022).
- [25] V. Wang, N. Xu, J.-C. Liu, G. Tang, and W.-T. Geng, Vaspkit: A user-friendly interface facilitating high-throughput computing and analysis using vasp code, *Computer Physics Communications* **267**, 108033 (2021).
- [26] Q. Wu, S. Zhang, H.-F. Song, M. Troyer, and A. A. Soluyanov, Wanniertools: An open-source software package for novel topological materials, *Computer Physics Communications* **224**, 405 (2018).
- [27] J. He, S. Ma, P. Lyu, and P. Nachtigall, Unusual dirac half-metallicity with intrinsic ferromagnetism in vanadium trihalide monolayers, *Journal of Materials Chemistry C* **4**, 2518 (2016).
- [28] Y. Zhou, H. Lu, X. Zu, and F. Gao, Evidencing the existence of exciting half-metallicity in two-dimensional ticl3 and vcl3 sheets, *Scientific reports* **6**, 19407 (2016).
- [29] C. Ouettar, H. Yahi, K. Zanat, and H. Chibani, Tuned electronic and magnetic properties in 3d transition metal doped vcl3 monolayer: a first-principles study, *Physica Scripta* **98**, 025814 (2023).
- [30] W. Klemm and E. Krose, Die kristallstrukturen von sccl3, ticl3 und vcl3, *Zeitschrift für anorganische Chemie* **253**, 218 (1947).
- [31] B. Shabbir, M. Nadeem, Z. Dai, M. S. Fuhrer, Q.-K. Xue, X. Wang, and Q. Bao, Long range intrinsic ferromagnetism in two dimensional materials and dissipationless future technologies, *Applied Physics Reviews* **5** (2018).
- [32] J. Yang, J. Wang, Q. Liu, R. Xu, Y. Li, M. Xia, Z. Li, and F. Gao, Enhancement of ferromagnetism for vi3 monolayer, *Applied Surface Science* **524**, 146490 (2020).
- [33] S. Tomar, B. Ghosh, S. Mardanya, P. Rastogi, B. Bhadoria, Y. S. Chauhan, A. Agarwal, and S. Bhowmick, Intrinsic magnetism in monolayer transition metal trihalides: A comparative study, *Journal of Magnetism and Magnetic Materials* **489**, 165384 (2019).
- [34] I. Žutić, J. Fabian, and S. D. Sarma, Spintronics: Fundamentals and applications, *Reviews of modern physics* **76**, 323 (2004).
- [35] G. Schmidt, D. Ferrand, L. Molenkamp, A. Filip, and B. Van Wees, Fundamental obstacle for electrical spin injection from a ferromagnetic metal into a diffusive semiconductor, *Physical Review B* **62**, R4790 (2000).
- [36] G. Xu, X. Zhang, Z. Hou, Y. Wang, E. Liu, X. Xi, S. Wang, W. Wang, H. Luo, W. Wang, *et al.*, New spin injection scheme based on spin gapless semiconductors: A first-principles study, *Europhysics Letters* **111**, 68003 (2015).
- [37] M. Ezawa, Quantized conductance and field-effect topological quantum transistor in silicene nanoribbons, *Applied Physics Letters* **102**, 172103 (2013).
- [38] Z. Zhang, X. Feng, J. Wang, B. Lian, J. Zhang, C. Chang, M. Guo, Y. Ou, Y. Feng, S.-C. Zhang, K. He, X. Ma, Q.-K. Xue, and Y. Wang, Magnetic quantum phase transition in cr-doped $bi_2(se_xte_{1-x})_3$ driven by the stark effect, *Nature nanotechnology* **12**, 953 (2017).
- [39] Y. Xu, Y.-R. Chen, J. Wang, J.-F. Liu, and Z. Ma, Quantized field-effect tunneling between topological edge or interface states, *Physical Review Letters* **123**, 206801 (2019).
- [40] M. Nadeem, I. Di Bernardo, X. Wang, M. S. Fuhrer, and D. Culcer, Overcoming boltzmann’s tyranny in a transistor via the topological quantum field effect, *Nano Letters* **21**, 3155 (2021).
- [41] M. S. Fuhrer, M. T. Edmonds, D. Culcer, M. Nadeem, X. Wang, N. Medhekar, Y. Yin, and J. H. Cole, Proposal for a negative capacitance topological quantum field-effect transistor, in *2021 IEEE International Electron Devices Meeting (IEDM)* (IEEE, 2021) pp. 38–2.
- [42] M. Nadeem, C. Zhang, D. Culcer, A. R. Hamilton, M. S. Fuhrer, and X. Wang, Optimizing topological switching in confined 2d-xene nanoribbons via finite-size effects, *Applied Physics Reviews* **9**, 011411 (2022).
- [43] S. Banerjee, K. Jana, A. Basak, M. S. Fuhrer, D. Culcer, and B. Muralidharan, Robust subthermionic topological

- transistor action via antiferromagnetic exchange, *Physical Review Applied* **18**, 054088 (2022).
- [44] B. Weber, M. S. Fuhrer, X.-L. Sheng, S. A. Yang, R. Thomale, S. Shamim, L. W. Molenkamp, D. Cobden, D. Pesin, H. J. Zandvliet, *et al.*, 2024 roadmap on 2d topological insulators, *Journal of Physics: Materials* **7**, 022501 (2024).
- [45] X.-L. Sheng and B. K. Nikolić, Monolayer of the 5 d transition metal trichloride oscl 3 : A playground for two-dimensional magnetism, room-temperature quantum anomalous hall effect, and topological phase transitions, *Physical Review B* **95**, 201402 (2017).
- [46] C. Huang, J. Zhou, H. Wu, K. Deng, P. Jena, and E. Kan, Quantum anomalous hall effect in ferromagnetic transition metal halides, *Physical Review B* **95**, 045113 (2017).
- [47] Q. Sun and N. Kioussis, Prediction of manganese trihalides as two-dimensional dirac half-metals, *Physical Review B* **97**, 094408 (2018).
- [48] J. He, X. Li, P. Lyu, and P. Nachtigall, Near-room-temperature chern insulator and dirac spin-gapless semiconductor: nickel chloride monolayer, *Nanoscale* **9**, 2246 (2017).
- [49] J.-Y. You, C. Chen, Z. Zhang, X.-L. Sheng, S. A. Yang, and G. Su, Two-dimensional weyl half-semimetal and tunable quantum anomalous hall effect, *Physical Review B* **100**, 064408 (2019).
- [50] Y.-p. Wang, S.-s. Li, C.-w. Zhang, S.-f. Zhang, W.-x. Ji, P. Li, and P.-j. Wang, High-temperature dirac half-metal pdcl 3 : a promising candidate for realizing quantum anomalous hall effect, *Journal of Materials Chemistry C* **6**, 10284 (2018).
- [51] J.-Y. You, Z. Zhang, B. Gu, and G. Su, Two-dimensional room-temperature ferromagnetic semiconductors with quantum anomalous hall effect, *Physical Review Applied* **12**, 024063 (2019).
- [52] J. Sun, X. Zhong, W. Cui, J. Shi, J. Hao, M. Xu, and Y. Li, The intrinsic magnetism, quantum anomalous hall effect and curie temperature in 2d transition metal trihalides, *Physical Chemistry Chemical Physics* **22**, 2429 (2020).
- [53] P. Li, Prediction of intrinsic two dimensional ferromagnetism realized quantum anomalous hall effect, *Physical Chemistry Chemical Physics* **21**, 6712 (2019).

Supplementary Information

Electronic dispersion and the role of entropy

Band dispersion of zero-entropy VCl_3 monolayer, 1×1 unit cell and 2×2 supercell, and entropic VCl_3 monolayer with a long-range order (LRO) along the zigzag chains [ZZ-ttt] is shown in figure **S1**. Unlike half-metallic character in zero-entropy monolayers, figure **S1(a-d)**, ZZ-ttt entropic configuration exhibits spin gapless semiconducting (SGS) behavior, where SOI opens a nontrivial energy gap leading to a fully gapped quantum anomalous Hall (QAH) phase, figure **S1(e,f)**. Figure **S2** shows band dispersion for other three LRO-entropic configurations, namely SL-t't't', Mix-t't't', and Mix-t'tt'.

In the LRO-entropic chiral structure [SL-t't't'], TM-atoms are substituted on the sublattice sites such that the triangular sublattice A is formed by V atoms and the triangular sublattice B is formed by M' (Ti, Cr, Fe, Co) atoms. In this configuration, an increase in entropy modifies nearest neighbor hopping between V atoms and the dopant M' atoms such that a gap is induced in the low-energy bands. As a consequence, the LRO-entropic chiral structure displays a gapped dispersion featuring a ferromagnetic insulating phase, as shown in figure **S2(a)**. Consistent with previous analysis for the ZZ-ttt configuration, entropy engineering drives band flattening along with a blue shift at K/K' points while a red shift across M-point. However, the bulk states across the Γ -point remain mostly unaffected, indicating a redistribution of various orbitals' contributions to the low-energy bands and the associated crystal fields. Furthermore, unlike the ZZ-ttt configuration that displays an intertwining between localization and de-localization of d-orbitals, localization wins over de-localization in the SL-t't't' configuration. On the other hand, in the Mix-t't't' LRO entropic configuration, de-localization dominates over localization and the band dispersion exhibits a nodal-line character between spin-up and spin-down bands, as shown in figure **S2(b)**. Interestingly, a small change in this configuration, induced by exchanging a sublattice site of one of the V atoms with a Cr atom, drastically changes the band dispersion, as shown in figure **S2(c)**. It shows that entropy engineering is an effective mechanism to control the bandstructure.

Detailed orbital resolved band dispersion of zero-entropy VCl_3 monolayer (1×1 unit cell) and the LRO-entropic VCl_3 monolayer ZZ-ttt (2×2 unit cell) are shown in figure **S3** and **S4**, respectively. In the zero-entropy VCl_3 monolayer, low-energy conduction band of the Dirac dispersion is predominantly occupied by the $d_{x^2-y^2}$ orbital, along with a contribution from the d_{xy} and d_{xy} orbitals along the M-K- Γ and K-M- Γ line, respectively. On the other hand, low-energy valence band of the Dirac dispersion is predominantly occupied by the d_{z^2} orbital, along with a small contribution from in-plane 3d orbitals ($d_{x^2-y^2}$ and d_{xy}) around the Dirac point. However, in the LRO-entropic ZZ-ttt configuration, the low-energy Dirac bands are completely occupied by the in-plane 3d orbitals ($d_{x^2-y^2}$ and d_{xy}) while the 3d orbitals with out-of-plane component (d_{z^2} , d_{yz} , d_{zx}) do not contribute to the states around the Fermi level in the spin-up channel. Orbital contributions from doped M' atoms are also depicted in figure **S4**.

| Sample | M_{V_1} | M_{V_2} | M_{V_3} | M_{V_4} | M_{V_5} | M_{V_6} | M_{V_7} | M_{V_8} | M_{Cl} | M_{total} |
|------------------------|-----------|-----------|-----------|-----------|-----------|-----------|-----------|-----------|----------|-------------|
| VCl ₃ (1x1) | 1.935 ↑ | 1.935 ↑ | - | - | - | - | - | - | ~ 0.03 ↓ | 4↑ |
| VCl ₃ (2x2) | 1.916 ↑ | 1.916 ↑ | 1.916 ↑ | 1.916 ↑ | 1.916 ↑ | 1.916 ↑ | 1.916 ↑ | 1.916 ↑ | ~ 0.03 ↓ | 16↑ |

TABLE I. Magnetic moments and spin orientations of V-atoms in zero-entropy VCl₃ monolayer. All values are given in μ_B .

Magnetic moments and local spin textures

As shown in tables I and II, local magnetic moments and local spin textures strongly depend on the level of entropy and the nearest-neighbor environment. In addition, the entropy-induced transformation of the ferromagnetic ground state, as well as the modification of electronic structure, can also be understood based on the differences between the number of valence electrons contributed from the M' atoms and those from the V atoms. For instance, like the ferromagnetic ground state of the VCl₃ monolayer with a total magnetic moment of 4 μ_B (16 μ_B for a 2 x 2 supercell), ground states of the LRO-entropic monolayers ZZ-ttt and SL-t't't' remain ferromagnetic, but the total magnetic moment reduces to 10.972 μ_B and 12.143 μ_B , respectively. In addition, local magnetic moments of individual TM cations and local spin textures strongly depend on the level of entropy and the type of LRO.

In the LRO-entropic monolayer ZZ-ttt, similar to the high-spin state of vanadium V³⁺ [3d²], the magnetic moments of Ti ($m_B \approx +0.413 \mu_B$) and Cr ($m_B \approx +2.738 \mu_B$) are found to be consistent with their respective value in the +3 oxidation state, i.e., Ti³⁺ [3d¹] and Cr³⁺ [3d³]. However, the magnetic moments of Co ($m_B \approx +0.582 \mu_B$) suggest that it is found in the low-spin state, Co²⁺ [3d⁷]. On the other hand, Fe atom contributes $m_B \approx -0.743 \mu_B$ to the total magnetic of the ZZ-ttt configuration, which is oppositely aligned to the magnetic moments of other TM cations. It suggests that Fe is found to be in the low-spin state Fe³⁺ [3d⁵] and the Cl↓-Fe↓-Cl↓ bond favors ferromagnetic interactions. This behavior of Fe in the LRO-entropic monolayer ZZ-ttt is completely different from that of Fe cations in Fe-doped low-entropy VCl₃ [29], where Fe³⁺ [3d⁵] is found to exist in a high-spin state ($m_B \approx +4.106 \mu_B$), enhancing the total magnetic moment of VCl₃ 2 x 2 monolayer from 16 μ_B to 19 μ_B , and the ferromagnetic nature of Cl↑-Fe↑-Cl↑ bond is indebted to the positive value of the local magnetic moment of the Cl atoms. The local spin texture of Fe and the deviation from a high-spin state in the low-entropy case to a low-spin state in the high-entropy case could be a consequence of the level of entropy and symmetry-breaking effects.

In the SL-t't't' configuration, low/high spin states of the TM cations remain the same as in the ZZ-ttt configuration. However, unlike the ZZ-ttt configuration, magnetic moments of all the TM cations remain positive, and thus an antiferromagnetic interaction is favored by all the Cl↓-TM↑-Cl↓ bonds, as indicated by the negative local magnetic moments of the Cl atoms. That is, the local spin textures are similar to that in the zero-entropy case. However, the magnetic moments of V atoms are further reduced from the zero-entropy case.

Local magnetic moments and local spin textures become more interesting in the LRO-entropic Mix-t't't and Mix-t'tt configurations. First, magnetic moments of two of the V atoms significantly reduced, down to +0.393 μ_B and +0.253 μ_B in the Mix-t't't configuration. Second, like the ZZZ-ttt and SL-t't't' configurations, Fe and Cr favor low-spin state and high-spin state, respectively. However, the local magnetic moments of both Fe and Cr are negative. Third, unlike the ZZZ-ttt and SL-t't't' configurations, the magnetic moments of Co ($m_B \approx +2.455 \mu_B$) suggest that it is found in a high-spin state, Co²⁺ [3d⁷].

In the LRO-entropic Mix-t'tt, on the other hand, magnetic moment of only one of the V atoms reduced to +0.421 μ_B while the other three shows $m_B \approx +1.9 \mu_B$. Interestingly, the reduced magnetic moment of that V atom appears to be negative, highly contrasting from other LRO-entropic configurations. In addition, while the magnetic moment of the low-spin Fe state remains negative, magnetic moment of the high-spin Cr state becomes positive. Furthermore, unlike Mix-t't't but like ZZZ-ttt and SL-t't't' configurations, the magnetic moments of Co ($m_B \approx +0.597 \mu_B$) suggest that it is found in the low-spin state, Co²⁺ [3d⁷]. The magnetic ground state of Mix-t't't and Mix-t'tt configurations stabilizes with a reduced total magnetic moment of $m_B = +3.286 \mu_B$ and $m_B = +8.747 \mu_B$, respectively. In both of these mix entropic configurations, positive magnetic moments for some of the Cl atoms while negative magnetic moments for the other Cl atoms suggest an intermingling of ferromagnetic and antiferromagnetic Cl↑↓-TM↑↓-Cl↑↓ bonds.

A momentous change in the local magnetic moments and spin textures in the LRO-entropic Mix-t't't and Mix-t'tt configurations show that the electronic and magnetic properties are significantly altered by the relocation of a single Cr atom, indicating the fragile impact of entropy engineering on electronic and magnetic properties.

| Sample | M_{V_1} | M_{V_2} | M_{V_3} | M_{V_4} | M_{Ti} | M_{Fe} | M_{Cr} | M_{Co} | M_{Cl} | M_{total} |
|------------|-----------|-----------|-----------|-----------|----------|----------|----------|----------|-----------------|-------------|
| ZZ-ttt | 1.918 ↑ | 1.876 ↑ | 1.822 ↑ | 1.783 ↑ | 0.413 ↑ | 0.743 ↓ | 2.738 ↑ | 0.582 ↑ | (0.001-0.034) ↓ | 10.972 ↑ |
| SL-t't't' | 1.863 ↑ | 1.849 ↑ | 1.779 ↑ | 1.697 ↑ | 0.485 ↑ | 0.533 ↑ | 2.748 ↑ | 0.552 ↑ | (0.001-0.036) ↓ | 12.143 ↑ |
| Mix-t't't' | 1.827 ↑ | 1.762 ↑ | 0.393 ↑ | 0.253 ↑ | 0.166 ↑ | 0.963 ↓ | 2.713 ↓ | 2.455 ↑ | (0.001-0.035) ↓ | 03.286 ↑ |
| Mix-t'tt | 1.948 ↑ | 1.946 ↑ | 1.902 ↑ | 0.421 ↓ | 0.402 ↑ | 0.849 ↓ | 2.777 ↑ | 0.597 ↑ | (0.001-0.033) ↓ | 08.747 ↑ |

TABLE II. Magnetic moments and spin orientations of TM cations in LRO-entropic $TiV_4CrFeCoCl_{24}$ monolayers. Shaded cells represent spin-down polarization (cyan), low/high spin states of TM atoms different from their usual high/low spin states (red), spin-down configuration of V in the low-spin state (purple), and the appearance of Cl atoms in both spin-up and spin-down states (gray). All values are given in μ_B .

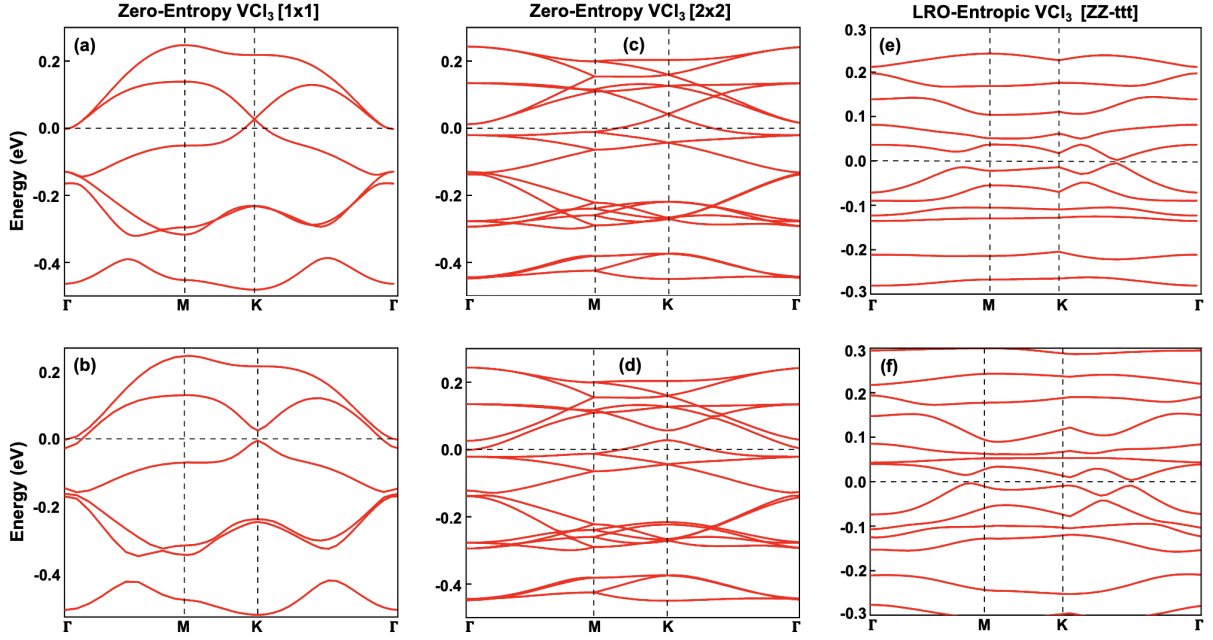


FIG. 5. [S1:] **Electronic dispersion of vanadium trichloride monolayer.** (a,b) Band dispersion of zero-entropy VCl_3 monolayer (1 x 1 unit cell) without SOI (a) and with SOI (b). (c,d) Band dispersion of zero-entropy VCl_3 monolayer (2 x 2 supercell) without SOI (c) and with SOI (d). (e,f) Band dispersion of entropic $TiV_4CrFeCoCl_{24}$ monolayer (2 x 2 supercell), with a long-range order along zigzag chains, without SOI (e) and with SOI (f).

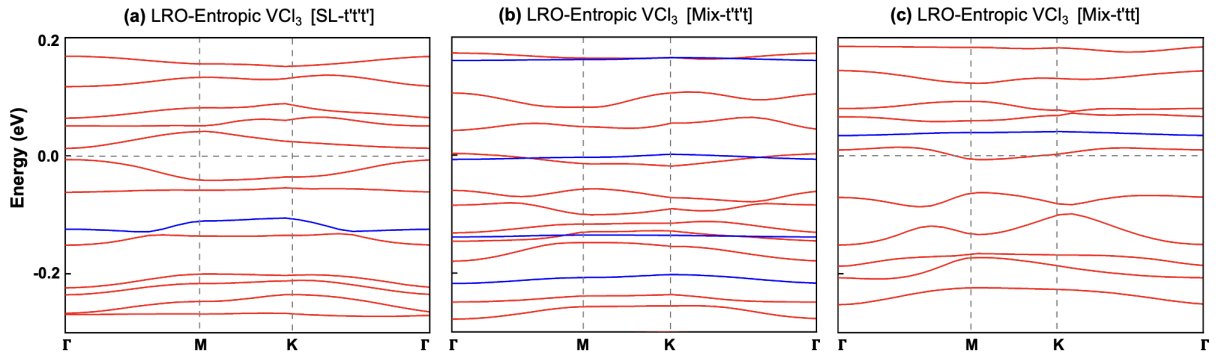


FIG. 6. [S2:] **Nearest neighbor effect on the electronic dispersion of LRO entropic VCl_3 monolayer.** Band dispersion of LRO entropic VCl_3 monolayer [SL-t't't'] (a) [Mix-t't't'] (b), and [Mix-t'tt]. Here red and blue bands represent spin-up and spin-down sectors, respectively.]

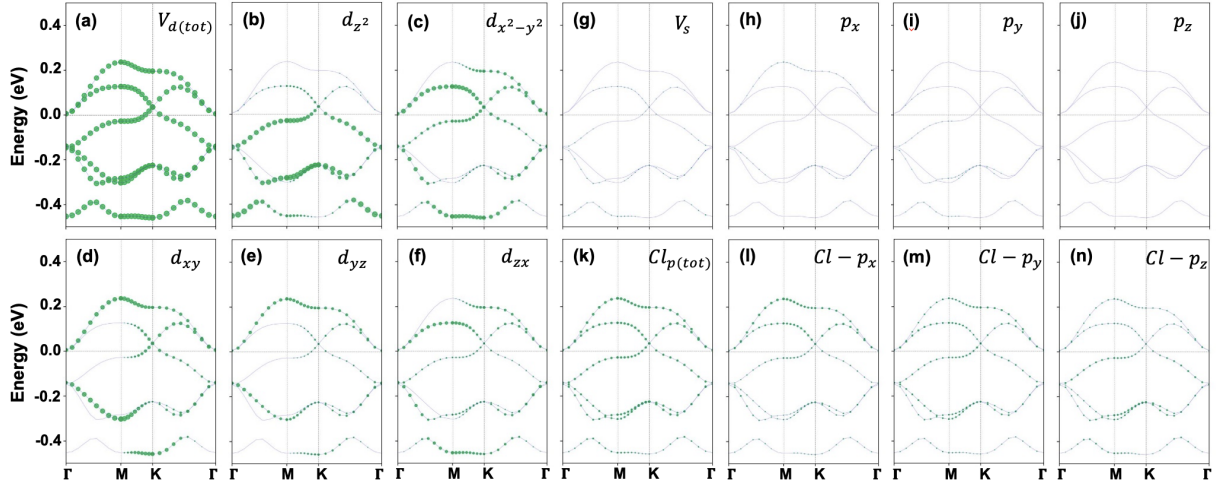


FIG. 7. [S3:] **Orbital resolved band dispersion of VCl_3 monolayer.** (a-f) Orbital contribution from d-orbitals of vanadium (a), e_g orbitals (d_{z^2} , $d_{x^2-y^2}$) (b,c) and t_{2g} orbitals (d_{xy} , d_{yz} , d_{zx}) (d,e,f). (g-j) Orbital contribution from s-orbitals (g) and p-orbitals (h,i,j) of vanadium. (k-n) Orbital contribution from p-orbitals of Cl. The size of the bands represents the orbital weight.

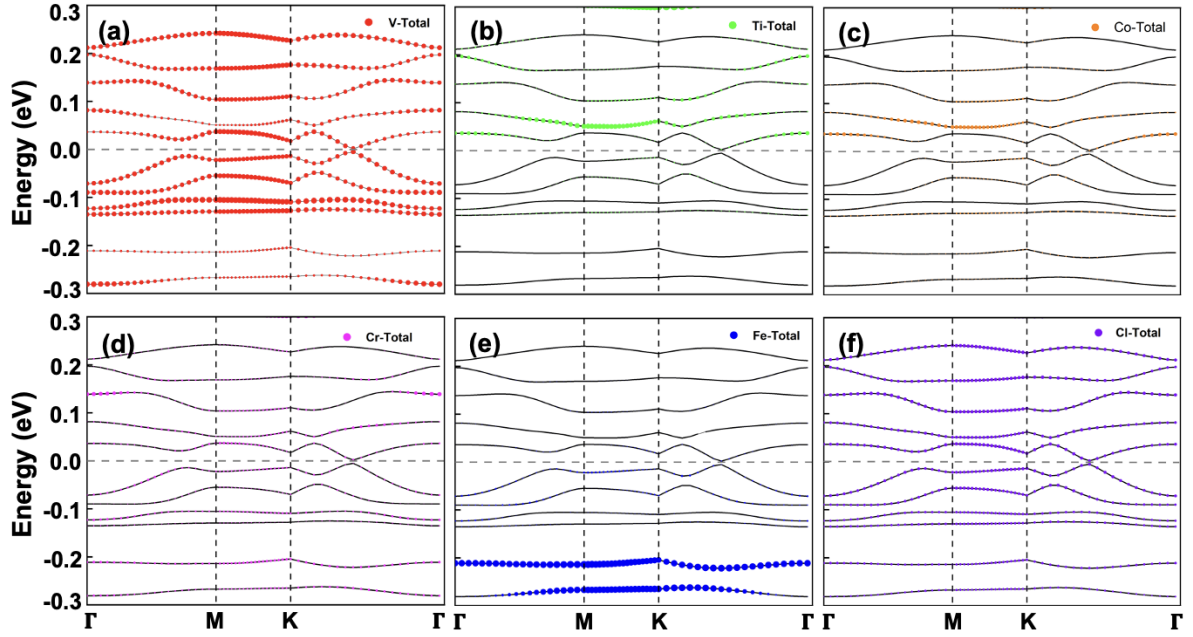


FIG. 8. [S4:] **Orbital resolved band dispersion of entropic VCl_3 monolayer.** (a-f) Orbital-resolved band structures in $TiV_4CrFeCoCl_{24}$ monolayer with the corresponding contribution from V (a), Ti (b), Co (c), Cr (d), Fe (e), and Cl (f) atoms, respectively. The size of the bands represents the orbital weight.